Bulletin of the Seismological Society of America, Vol. 100, No. 3, pp. 995–1009, June 2010, doi: 10.1785/0120090211

Tsunami Simulations of the 1867 Virgin Island Earthquake: Constraints on Epicenter Location and Fault Parameters

by Roy Barkan and Uri ten Brink

Abstract The 18 November 1867 Virgin Island earthquake and the tsunami that closely followed caused considerable loss of life and damage in several places in the northeast Caribbean region. The earthquake was likely a manifestation of the complex tectonic deformation of the Anegada Passage, which cuts across the Antilles island arc between the Virgin Islands and the Lesser Antilles. In this article, we attempt to characterize the 1867 earthquake with respect to fault orientation, rake, dip, fault dimensions, and first tsunami wave propagating phase, using tsunami simulations that employ high-resolution multibeam bathymetry. In addition, we present new geophysical and geological observations from the region of the suggested earthquake source. Results of our tsunami simulations based on relative amplitude comparison limit the earthquake source to be along the northern wall of the Virgin Islands basin, as suggested by Reid and Taber (1920), or on the carbonate platform north of the basin, and not in the Virgin Islands basin, as commonly assumed. The numerical simulations suggest the 1867 fault was striking 120°–135° and had a mixed normal and left-lateral motion. First propagating wave phase analysis suggests a fault striking 300°–315° is also possible. The best-fitting rupture length was found to be relatively small (50 km), probably indicating the earthquake had a moment magnitude of ~7.2. Detailed multibeam echo sounder surveys of the Anegada Passage bathymetry between St. Croix and St. Thomas reveal a scarp, which cuts the northern wall of the Virgin Islands basin. High-resolution seismic profiles further indicate it to be a reasonable fault candidate. However, the fault orientation and the orientation of other subparallel faults in the area are more compatible with right-lateral motion. For the other possible source region, no clear disruption in the bathymetry or seismic profiles was found on the carbonate platform north of the basin.

Introduction

The 1867 Virgin Islands earthquake and tsunami are examples of a natural disaster that changed the course of local history. At the time of the event, the United States was engaged in the purchase of the then Danish Virgin Islands and had sent three navy ships to explore the islands. The devastating tsunami, which caused loss of lives and damage to the navy ships, was among the reasons that the purchase was postponed for another 50 yrs (e.g., Dookhan, 1975). However, the presence of navy ships in St. Thomas and St. Croix at the time of the earthquake and tsunami also resulted in relatively accurate reports by the ships' commanding officers of water level and timing of events. Reid and Taber (1920) summarized these reports and used them to locate the possible epicenter between St. Thomas and St. Croix. The 18 November 1867 earthquake consisted of two mainshocks, about 10 min apart in the same general area (Reid and Taber, 1920). The shaking was most severe in St. Thomas and almost as severe in St. Croix. Reid and Taber (1920) estimated earthquake intensity IX (using Rossi–Forel scale) at these two islands and at Tortola, St. John, Vieques, and Culebra, and lower intensity in eastern Puerto Rico, Virgin Gorda, and the northern Lesser Antilles. A tsunami wave closely followed the shocks and had significant effects in Puerto Rico, the Virgin Islands, the Lesser Antilles, and Venezuela (Table 1 and Fig. 1; Reid and Taber, 1920; O'Loughlin and Lander, 2003; Zahibo *et al.*, 2003). With the exception of Guadeloupe, the highest run-up reports were from St. Thomas and western St. Croix.

The 1867 earthquake is likely a manifestation of tectonic deformation of the Anegada Passage. The Anegada Passage cuts across the Antilles arc between the Virgin Islands and the Lesser Antilles. It is the only deep-water passage between the Atlantic Ocean and the Caribbean Sea where Atlantic intermediate water can enter the Caribbean (Fratantoni *et al.*, 1997). The passage has a complex bathymetry with irregular ridges reaching 40 m below sea level and irregular basins

Table 1

Sites of Historical 1867 Tsunami Run-Up Reports

	Site	Reported Run-up* (m)	Relative Amplitude† Observed	Relative Amplitude† Calculated	j‡	Calculated Location§ Longitude (°E)	Calculated Location§ Latitude (°N)	Sources*	Travel Time‖ (min) Reported	Travel Time‖ (min) Calculated
St. Thomas	Hassel Island	4.9	1	1.462	0	−64.933	18.27	Za, Rei	0–10	9
	Charlotte Amalie	6				−64.953	18.315	Za, Rei		
St. Croix	Frederiksted	7.6				−64.886	17.708	Za, Rei	0–10	4
	North West		1.2667	1.613	1	−64.87	17.782			
Puerto Rico	Vieques	High waves				−65.382	18.095	Za, Rei	0	11
	Culebra					−65.29	18.26	OL, Rei		
	Arroyo	1.5				−66.064	17.91	OL, Za, Rei		
	Salinas					−66.285	17.87	OL		
	Yabucoa	2 (IH#)	0.333	0.382	2	−65.818	18.007	Za, Rei		
	Fajardo	Very small				−65.833	18.001	Rei		
British VI	Virgin Gorda					−64.444	18.402	OL		7.5
	Peter Island	1.5	0.3	0.596	3	−64.581	18.322	Za, Rei		
	Tortola**	1.5				−64.647	18.32	Za, Rei		
Leeward Islands	St. Martin					−63.075	18.017	OL		30.5
	St. Bart					−62.88	17.875	OL, Rei		
	Saba	High waves				−63.254	17.635	Za, Rei		
	Barbuda	1.4	0.28	0.390	4	−61.9	17.626	OL		58
	St Kitts	2.4	0.48	0.436	5	−62.8	17.337	OL, Za		
	Montserrat					−62.24	16.78	OL		
	St. John's, Antigua	3 (IH#)	0.5	0.386	6	−62	17.119	Za, Rei		61.5
Guadeloupe	Basse Terre	2	0.4	0.415	7	−61.712	15.993	Za, Rei	0–10	
Dominica	Prince Rupert's Bay	3				−61.476	15.56	OL		59
Martinique		Reported								73
St. Lucia	Anse la raye	1.2				−61.062	13.938	Za, OL		
St. Vincent	Cumberland Bay	0.6	0.12	0.404	8	−61.3	13.255	OL		78
Grenadines	Admiralty Bay	1.8	0.333	0.416	9	−61.31	13	Za, OL		
Grenada	St. George's	1.5	0.3	0.512	10	−61.77	12.119	Za, Rei	120–140	84
Venezuela	Isle de Margarita	Reported				−64	11.226	Za, Rei		

*Run-up reports are from Reid and Taber, 1920 (Rei); Zahibo *et al.*, 2003 (ZA); O'Loughlin and Lander, 2003 (OL).

†Observed relative amplitude for χ^2 analysis is normalized to St. Thomas, outside the harbor (see the section A Method to Quantitatively Compare between Possible Epicenters and Fault Rupture Parameters for details). Calculated relative amplitude is from RF (see the section The 1867 Earthquake Suggested Epicenter and Fault Parameters for details).

‡Column j depicts the historical sites that were used for χ^2 analysis (see the section A Method to Quantitatively Compare between Possible Epicenters and Fault Rupture Parameters for details). Numbers 0–3 and 4–10 are in areas of HRES and LRES bathymetric grid, respectively (see the Tsunami Model Simulations section for details).

§The coordinates (longitude and latitude) indicate the center of the group of grid points where the amplitude was calculated (see the Tsunami Amplitude section for details).

‖Travel time-first arrival phase after estimated time of earthquake (see the section Geophysical Evidence for the 1867 Earthquake Suggested Epicenter, for details).

#IH, in harbor.

**The calculated point for Tortola is between St. John, U.S. Virgin Islands, and Peter Island because the numerical model could not propagate the tsunami through the shallow water and dispersed islands.

reaching a depth of 4500 m (Fig. 1). Relative motion across the Anegada Passage has been suggested to be left-lateral transtension (Hess and Maxwell, 1953; Gill *et al.*, 1999; ten Brink, 2005), perpendicular extension (Murphy and McCann, 1979), or right-lateral transtension (Jany *et al.*, 1990), but earthquake activity and geodetic GPS velocities have hitherto been too low to define the sense and rate of motion. Hence, defining the rupture parameters of the 1867 earthquake may help constrain the motion across the Anegada Passage.

A few attempts have been made to characterize the 1867 earthquake based on the orientation of the wall of the Virgin Islands basin, tsunami arrival time, earthquake shaking intensity, and numerical modeling of the tsunami (Reid and Taber, 1920; Lander *et al.*, 2002; Zahibo *et al.*, 2003). The origin of the earthquake is most commonly assumed to be in the Virgin Island basin between St. Croix and St. Thomas (Fig. 1). Two major solution faults were previously proposed and will be referred to later on in this article as

- Reid fault (RF): Reid and Taber (1920) suggested an epicenter located on the north wall of the Virgin Island basin not far from latitude 18.16667° N and longitude 65.0° W (epicenter 14 in Figs. 1 and 2). They hypothesized an east–west trending fault, several tens of kilometers long, located 16–17 km south of St. Thomas along the northern wall of the Virgin Island basin and having a slip < 10 m, as a possible candidate.

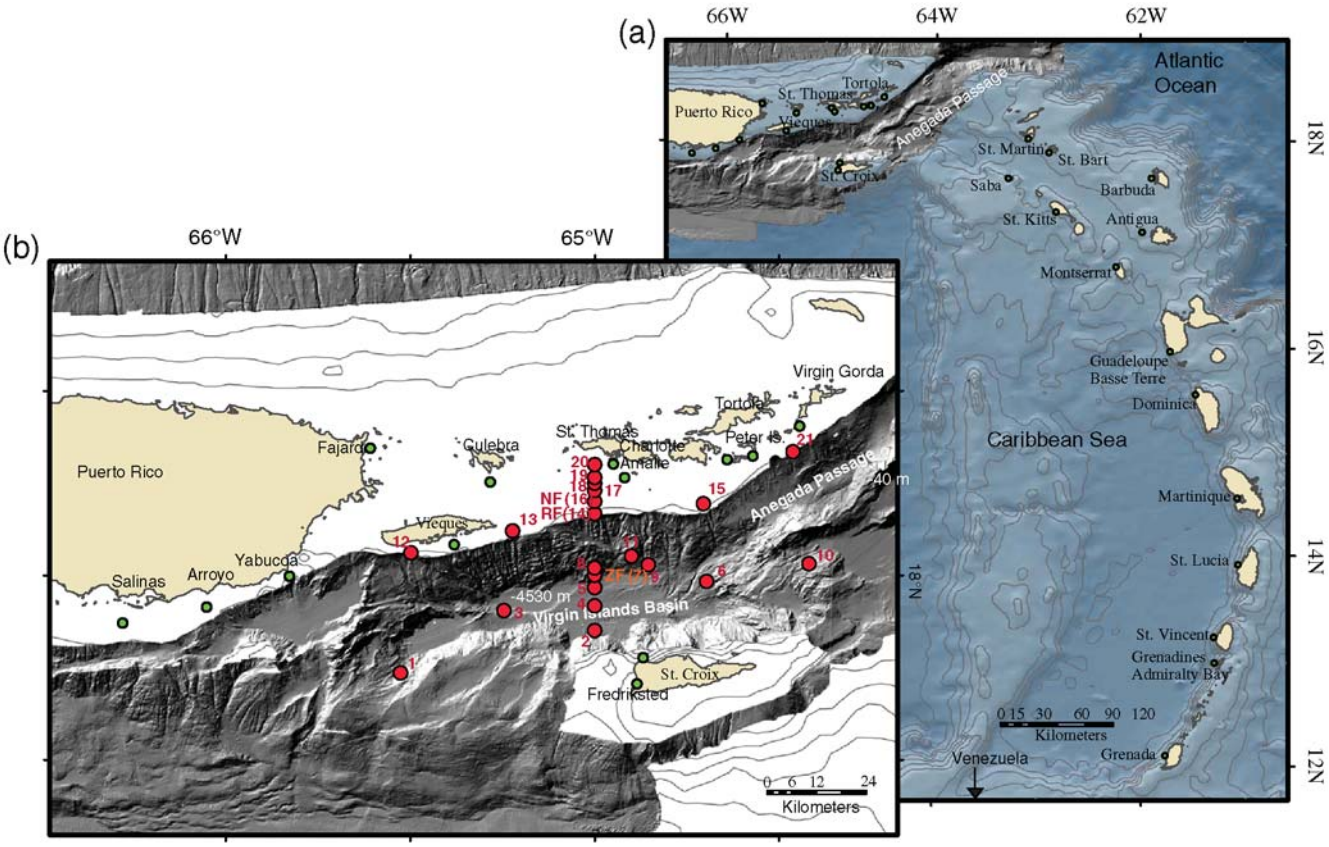

Figure 1. (a) Locations of run-up reports in Table 1. Shaded blue bathymetry is referred to as LRES bathymetry in the text. Multibeam bathymetry is referred to as HRES bathymetry in the text. Contour interval is 500 m. (b) Bathymetric map of the Virgin Islands and Puerto Rico regions. Earthquake sources (placed in the center of finite faults) used to generate tsunami simulations are shown in red circles with corresponding fault model number (see Table 2 for source coordinates and fault parameters). Locations of detailed near source run-up reports in Table 1 are also shown as green dots. RF, refers to a scarp that may correspond to our hypothesized RF (see The 1867 Earthquake Suggested Epicenter and Fault Parameters section for details); VIB, Virgin Island basin; NF, North fault (see text for details).

- Zahibo fault (ZF): Zahibo *et al.* (2003) suggested a 120 × 30 km thrust fault (rake of 90°) located within the Virgin Islands basin at 18.0° N and 65.0° W and oriented N75°E (epicenter 7 in Figs. 1 and 2). The dip angle, focal depth, and displacement selected for their hydrodynamic modeling were 70°, 3000 m, and 8 m, respectively.

In this article, we first constrain the epicenter of the 1867 earthquake using tsunami simulations that utilize newly collected high-resolution (HRES) multibeam bathymetry (refer to the Methodology section for more details). Features such as fault orientation, rake, dip, and fault dimensions are then tested, taking into account empirical relationships between earthquake magnitude and fault parameters, relative plate motion, and first wave propagating phase. Finally, we present geophysical and geological observations from the region of the suggested earthquake source and discuss locations of possible faults and their relationship to the overall tectonic deformation of the Anegada Passage.

Constraining source location and fault parameters based on tsunami travel time is problematic (Zahibo *et al.*, 2003; Barkan *et al.*, 2009) due to the inaccuracy of historical reports, due to the possibility of localized landslide-generated tsunamis triggered by the earthquake, and due to the difficulties in simulating tsunami propagation at shallow depths (see the following sections, Tsunami Model Simulations and Tsunami Amplitude). The exact time of the 1867 earthquake is uncertain. Reports indicate it was between 14:30 and 15:00 o'clock (Reid and Taber, 1920; O'Loughlin and Lander, 2003). For a tsunami traveling in deep water (i.e., the long-wavelength limit) at a phase speed of $\sqrt{gh}$ (where g is the acceleration due to gravity and h is the water depth), such a difference in origin time makes correlation between simulated arrival times and historical arrival times highly inaccurate. Furthermore, Reid and Taber (1920) suggested that the unreasonably high reported run-up at Guadeloupe and seemingly immediate arrival time of the tsunami (15:00) may be attributed to a nearby landslide. Zahibo *et al.* (2003) agree with this suggestion, arguing that the report in Guadeloupe was a result of a local amplification of the wave. Because of the previously discussed reasons, direct constraining of source location and fault parameters based on tsunami travel time was not attempted in this study. Nevertheless, the tsunami arrival times depicted in the marigrams

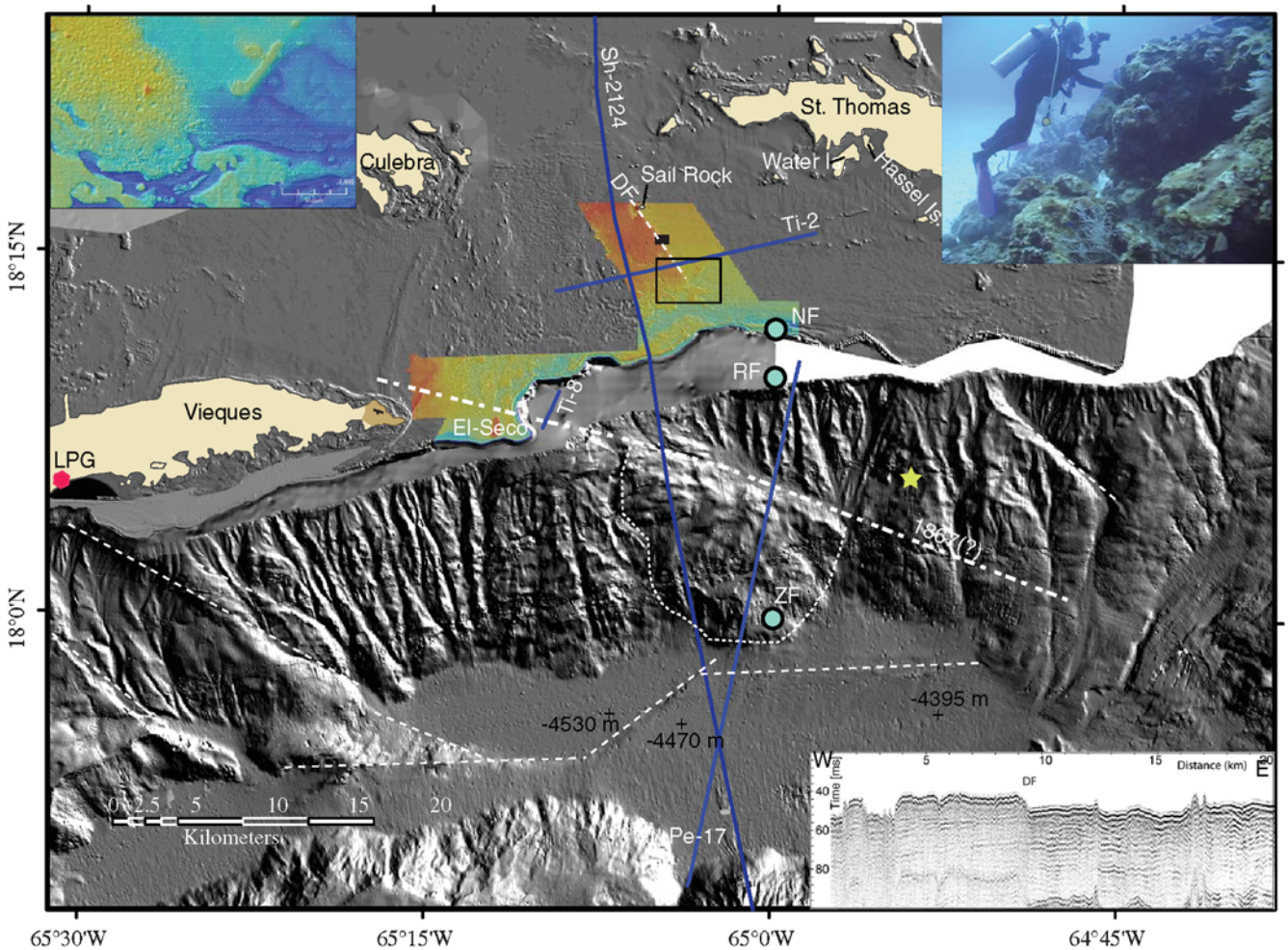

Figure 2. Shaded bathymetry map of the Virgin Islands basin and the Virgin Islands platform. Blue lines indicate locations of seismic profiles shown at the bottom right corner and in Figure 10. Heavy dashed line indicates the proposed location of the fault rupture of the 1867 earthquake and tsunami. Thin dashed lines represent other possible active faults in the area. The dotted line encloses the area of morphological disturbance in the basin wall below the proposed 1867 fault rupture. The brown area at the eastern end of Vieques indicates the uplifted and tilted Pleistocene platform (Meyerhoff, 1926). The black rectangle shows the location of dive. Yellow star is the location of earthquake swarms in 1978–1979 (Frankel *et al.*, 1980). NF, RF, and ZF are the central locations of fault sources used in the tsunami simulations. DF is the fault trace proposed by Donnelly (1965). Top right inset: dive along the proposed fault scarp by Donnelly (1965). Note that the slope is covered by well-developed lettuce corals. Photo taken by Drex Harrington. Bottom right inset: part of single-channel seismic line Ti-2 collected by a mini-sparker in 2009. Note the lack of offset along the proposed fault by Donnelly (DF). Top left inset: enlargement of the multibeam bathymetry in the region marked by an open black rectangle. LPG, location of Laguna Playa Grande where Woodruff *et al.* (2008) did not find distinct tsunami deposits from 1867.

(Fig. 7) generated from the simulated RF (Table 1, calculated travel time) are reasonable with respect to historical arrival time reports (Table 1, reported travel time).

Methodology

Tsunami Model Simulations

All simulations presented in this article were generated using COMCOT (Cornell Multigrid Coupled Tsunami Model; Liu *et al.*, 1998; Lynett *et al.*, 2002). COMCOT solves both linear shallow water and nonlinear shallow water equations in spherical coordinates. Aside from the governing equations, the linear versus nonlinear hydrodynamic models, as implemented in COMCOT, also differ in the coastal boundary conditions. The linear model uses reflective boundary conditions and is therefore unable to perform explicit run-up calculations at the shallow water areas along the coast. The COMCOT nonlinear model uses moving boundary conditions and is capable of more accurate wave amplitude calculations closer to shore. The latter model was therefore used in this article. In principle, numerical computation of wave heights based on shallow water equations is sufficient and accurate as long as the modeled tsunami wavelength is much greater than water depth and the wave amplitude is much smaller than water depth. This principle holds up until the deep part of the continental shelf. Consequently, this

article is unable to provide definite run-up results and only relative amplitudes can be considered.

The input depth file contains the bathymetry of the region where the simulation took place. Tsunami propagation is highly influenced by seafloor bathymetry (e.g., Matsuyama *et al.*, 1999; Mofjeld *et al.*, 2000). HRES bathymetric grids are therefore essential for accurate modeling. Two different bathymetric grids were used for all simulations: a 394× 476 low-resolution (LRES) bathymetry grid with 1 arcmin resolution covering the entire area of interest (from −67.052067° W to −60.4723° W and from 11° N to 18.933° N) (LRES, shaded blue bathymetry; Fig. 1a), and an overlapping 415 × 840 bathymetry grid (HRES) with 12 arcsec resolution covering the near source area (from −67.035005° W to −64.2354° W and from 17.5166015° N to 18.8999° N) (HRES, multibeam bathymetry; Fig. 1b). The output file used for all interpretations in this article is the maximum wave amplitude file. This file contains the calculated maximum sea level amplitude for a selected region, throughout an entire simulation run (tsunami propagation time of 95 min or 5700 1 sec timesteps).

Tsunami Amplitude

To calculate wave amplitude, we averaged the amplitudes of five or nine model grid points at shelf locations: three (or five) adjacent points lined in a north–south direction and three (or five) adjacent points lined in an east–west direction, with common center points, whose coordinates are listed in Table 1. Points with zero wave amplitude or a depth shallower than 9 m were discarded from the average calculations. The groups of calculated points consisted of five points at sites located in the Lesser Antilles, where only the LRES grid was available, and nine points at sites in the Virgin Islands and Puerto Rico, where the HRES grid was available. Because tsunami amplitude is strongly dependent on water depth (Liu *et al.*, 1998; Ward, 2002), all amplitudes were normalized to depths of 40 m and 100 m prior to averaging using Green's law (Green, 1837):

$$h_1 = \left(\frac{b_0}{b_1}\right)^{1/2}\left(\frac{d_0}{d_1}\right)^{1/4} h_0, \qquad (1)$$

where, respectively, d_0 and b_0 are the measured water depth at the location and the angular section width of the propagating wave, d_1 and b_1 are the water depth and the angular section width at the site where the wave amplitude is to be approximated (40 m and 100 m in this case), and h_0 and h_1 are the corresponding wave amplitudes at these two locations. Because the distance between the computed and approximated locations in this study was reasonably short, the angular section width of the propagating wave was considered to remain constant, and equation (1) reduces to

$$h_1 = \left(\frac{d_0}{d_1}\right)^{1/4} h_0. \qquad (2)$$

The normalization of wave heights following equation (2) ensures a reliable comparison between the sites.

A Method to Quantitatively Compare between Possible Epicenters and Fault Rupture Parameters

Direct comparison between historical tsunami run-up reports and hydrodynamic model predictions with different epicenters and fault rupture parameters is difficult for the following reasons. First, historical eyewitness reports are not always reliable; second, our model does not calculate actual run-ups (see the Tsunami Model Simulations section); and third, run-up is sensitive to near-shore bathymetry and onshore topography. To overcome these limitations, the following method was used.

Estimated sea level changes (by officers on moored U.S. naval ships in Charlotte Amalie and Frederiksted harbors) and run-ups (by eyewitnesses onshore) of the 1867 tsunami were used for the analyses (Reid and Taber, 1920; O'Loughlin and Lander, 2003; Zahibo *et al.*, 2003). All observed run-up heights were scaled to Hassel Island at the entrance of Charlotte Amalie harbor, St. Thomas, because of the elaborate and consistent U.S. naval reports from that location (Reid and Taber, 1920; O'Loughlin and Lander, 2003). In order to account for the magnifying effect that harbors have on tsunami amplitude, we used the ratio between Charlotte Amalie (inside harbor) to Hassel Island (outside harbor) given by the naval reports as an empirical magnification ratio for all other historical locations. (Different harbor responses will, of course, have slightly different magnifications, but in the absence of information from other harbors, we use a single ratio). All run-ups reported inside the harbor (St. Croix, for instance) were decreased using the previously mentioned ratio to give the outside harbor amplitude. The outside harbor amplitudes were later compared to that of St. Thomas and are depicted in Table 1 (relative amplitude, χ^2). In order to quantitatively determine which epicenter best fits the historical reports with respect to location, fault strike, fault rake, and fault dimensions, we used a chi-squared minimization scheme,

$$\chi_i^2 = \sum_{j=1}^{10}\left(\mathrm{Amp}_{\mathrm{table}_j} - \frac{\mathrm{Amp}_j^i}{\mathrm{Amp}_0^i}\right)^2 / \mathrm{Amp}_{\mathrm{table}_j}, \qquad (3)$$

where i represents the 21 model epicenter locations (Fig. 1 and Table 2). $\mathrm{Amp}_{\mathrm{table}_j}$ is the relative amplitude (χ^2) reported at location j (see column labeled j in Table 1). These 10 locations along the coasts were chosen because the historical run-up reports at these locations were consistent among sources (Reid and Taber, 1920; O'Loughlin and Lander, 2003; Zahibo *et al.*, 2003). Amp_j^i is the amplitude generated by epicenter i at site j and Amp_0^i is the calculated amplitude at Hassel Island, St. Thomas. The best-fitting source should minimize the chi-squared value.

Chi-squared values calculated when depth was normalized to 40 m and 100 m showed similar results; Figures 3–5

Table 2
Geographical Coordinates and Fault Parameters of Source Locations as shown in Figure 2

Source	Longitude (°E)	Latitude (°N)	Length (km)	Width (km)	Slip (m)	Strike (°)	Rake (°)	Dip (°)
1	−65.5259	17.735	80	35	2	110	−90	60
2	−65	17.85	60	25	5	75	−90	45
3	−65.2463	17.90417	80	35	2	110	−90	60
4	−65	17.9167	varying	varying	varying	varying	varying	varying
5	−65	17.9667	80	35	2	110	−90	60
6	−64.6972	17.9833	80	35	2	110	−90	60
ZF (7)	−65	18	varying	varying	varying	varying	varying	varying
8	−65	18.02	60	35	2.667	all	−90	60
9	−64.8543	18.02783	80	35	2	110	−90	60
10	−64.419	18.031	80	35	2	110	−90	60
11	−64.9	18.052	60	25	5	110	−90	45
12	−65.498	18.061	60	25	5	78	−90	45
13	−65.222	18.12	60	25	5	75	−90	45
RF (14)	−65	18.1667	varying	varying	varying	varying	varying	varying
15	−64.705	18.194	60	25	5	78	−90	45
NF (16)	−65	18.2	varying	varying	varying	varying	varying	varying
17	−65	18.23	60	25	5	75	−90	45
18	−65	18.25	80	35	2	110	−90	60
19	−65	18.265	80	35	2	110	−90	60
20	−65	18.3	80	35	2	110	−90	60
21	−64.462	18.335	60	25	5	110	−90	45

Source locations are measured in the center of each finite fault. Source depth for all faults is 1000 m, taken at the top of the fault plane.

were created using equation (3) for amplitudes normalized to 40 m.

Results and Discussion

Figure 1 and Table 2 show and list all 21 earthquake sources that were modeled. All fault parameters roughly matched the empirical relationships depicted in Wells and Coppersmith (1994) for an M_w 7–7.5 earthquake. The initial perturbation of sea surface height was assumed to be similar to the seafloor perturbation from a calculated elastic dislocation model of fault rupture. The upper end of the fault plane was assumed to reach 1 km below the surface to avoid singularities in the rupture surface. The rake and strike angles follow the convention by Aki and Richards (1980).

Source Location

The first set of simulations was designed to constrain the fault location. A fault strike of 110° was chosen for these simulations, which is the orientation of a suspected fault along the northern wall of the basin, shown in the multibeam bathymetry data as an interruption to the canyon system (heavy dashed line marked 1867? in Fig. 2). Figure 3 compares source locations at different longitudes and latitudes based on the method outlined in the section, A Method to Quantitatively Compare between Possible Epicenters and Fault Rupture Parameters, and indicates that the best-fit source is located around 65° W and 18.1667–18.3° N. In other words, the best source location is along the northern wall of the Virgin Islands basin, as suggested by Reid and Taber (1920) or on the carbonate platform north of the basin. The northern wall of the Virgin Island basin is also associated with microseismic activity, whereas the floor of the basin and its southern wall are not (Murphy and McCann, 1979). Two shallow (~15 km) earthquake swarms occurred in November and December 1978 at 18.1° N, 64.9° W (Frankel *et al.*, 1980), which is close to the morphological expression of the possible 1867 rupture (yellow star in Fig. 2).

Fault Parameters: Strike, Rake, Fault Dimensions, and Earthquake Magnitude

The second set of simulations was designed to examine possible fault parameters based on the criteria developed in the section, A Method to Quantitatively Compare between Possible Epicenters and Fault Rupture Parameters. A fault located at source 14 (RF; Figs. 1 and 2 and Table 2) was chosen for this set because it is the southernmost epicenter in the group of favorable epicenters determined in the previous section (Fig. 3b). As such it minimized topographic interference by islands when we tested different fault orientations. In order to determine possible strike orientations, the fault strike was rotated between 65° and 140°. Figure 4a shows that fault strikes ranging from 120° to 140° fit better than the previously suggested east–west trending RF and ZF. Figure 4b shows a comparison between different fault dimension combinations (length × width × slip) that yield an M_w ~7.5 earthquake. McCann (1985) suggested a surface-wave magnitude, M_S 7.5, based on Reid and Taber (1920) observations of similar intensity and maximum felt distance for the 1867 Virgin Islands earthquake and for the 1918 western Puerto Rico earthquake and based on his magnitude estimate of

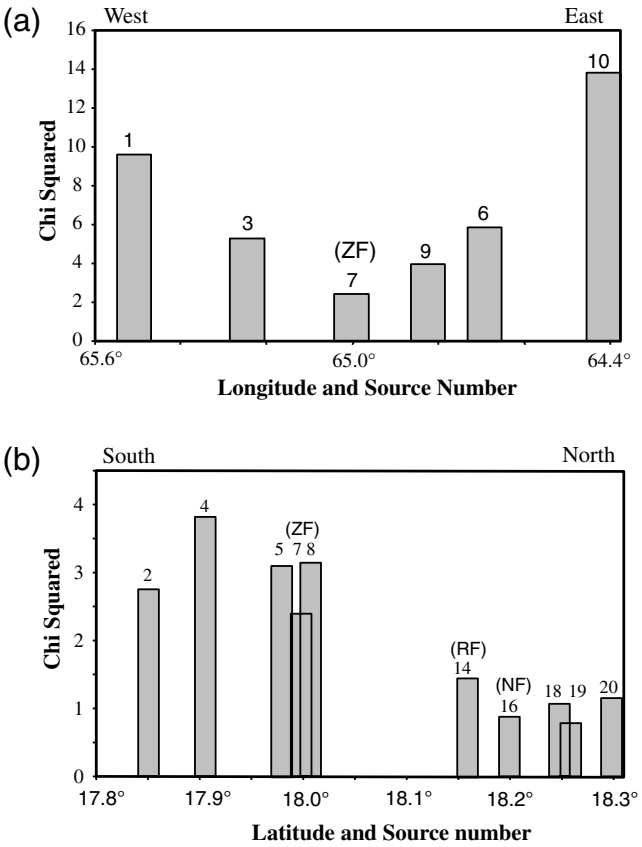

Figure 3. χ^2 comparison between fault sources that vary in (a) longitude and (b) latitude. Location of sources is shown in Figure 2 and listed in Table 2. Smaller bars represent sources that are better fitting to the 1867 Virgin Island epicenter (see the section A Method to Quantitatively Compare between Possible Epicenters and Fault Rupture Parameters for explanation). According to this test, source 7 (longitude 65° E) is the best-fitting candidate in longitude; locations between source 14 (latitude 18.1667° N) and source 20 (latitude 18.3° N) are the best-fitting candidates in latitude.

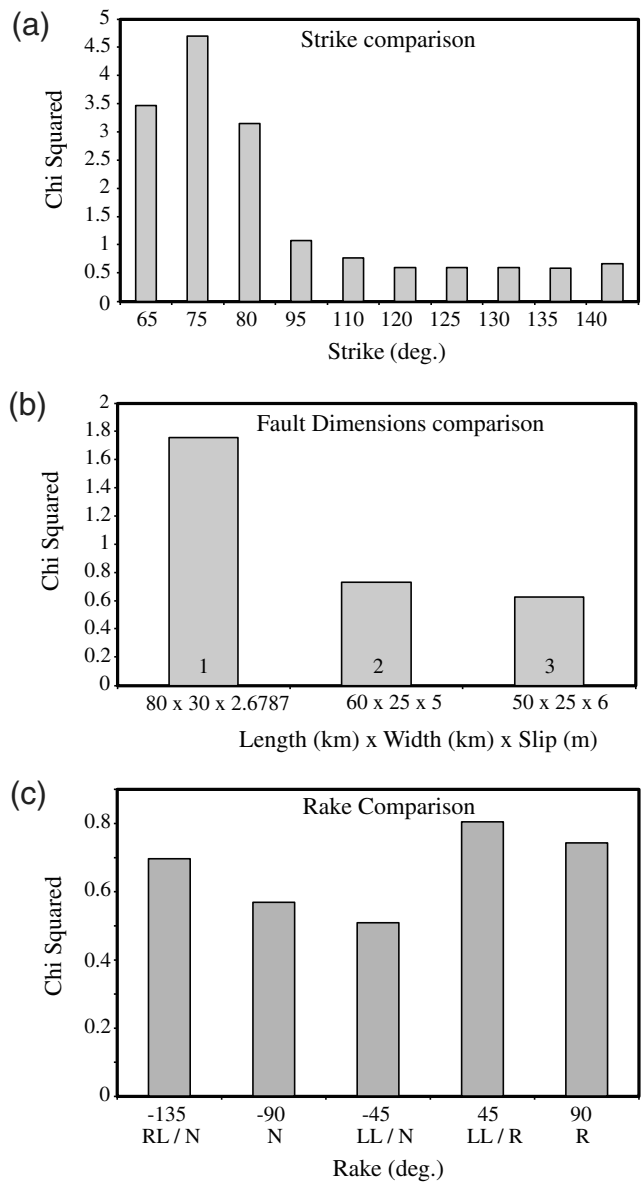

Figure 4. χ^2 comparison between tsunami amplitudes for different fault parameters located in source 14 (see Fig. 2 and Table 2). The parameters include (a) variations in fault strike, (b) combinations of fault dimensions (length × width × slip), and (c) rake. Smaller bars represent fault parameters that are better fitting to the 1867 Virgin Island fault parameters (see the section A Method to Quantitatively Compare between Possible Epicenters and Fault Rupture Parameters for explanation). According to this test, strike angles ranging from 120° to 140°, a combined left-lateral (LL) and normal (N) slip, a rake of −45°, and a relatively small earthquake area with a relatively large slip (combination number 3) best describe the 1867 Virgin Island earthquake. R is reverse slip.

M 7.5 for the 1918 earthquake. From this analysis, a smaller fault area with larger slip (combination number 3), that is, a larger stress drop, best fits the historical reports. Empirical relationships (Wells and Coppersmith, 1994) indicate that the length and width of the fault in combination number 3 fit a smaller magnitude earthquake (M 7.2). The suggested slip of 6 m fit an M_w ~7.5 earthquake according to the same empirical relationships. However, the log–linear correlation between average displacement (slip) and earthquake magnitude (Wells and Coopersmith, 1994) is much weaker ($r = 0.75$) and has a larger standard deviation ($s = 0.36$) than the correlation between rupture length or rupture width and magnitude ($r = 0.94, 0.84$; $s = 0.16, 0.15$). Therefore, using fault length and width to estimate the 1867 earthquake magnitude is probably more reliable than using its slip, indicating that the magnitude might have been closer to M 7.2. This conclusion agrees with later analyses of the 1918 western Puerto Rico earthquake, which revised its magnitude to M_S 7.3 (Pacheco and Sykes, 1992) and M_w 7.2 (Doser *et al.*, 2005).

Figure 4c compares between different fault rakes. The best-fit fault rake has an equal mix of strike slip and normal component (−45°), which is in agreement with previous suggestions of left-lateral transtension (ten Brink, 2005) and perpendicular extension (Murphy and McCann, 1979). However, fault orientation and the orientation of other faults in the area (Fig. 2) are more compatible with a mixed right-lateral and

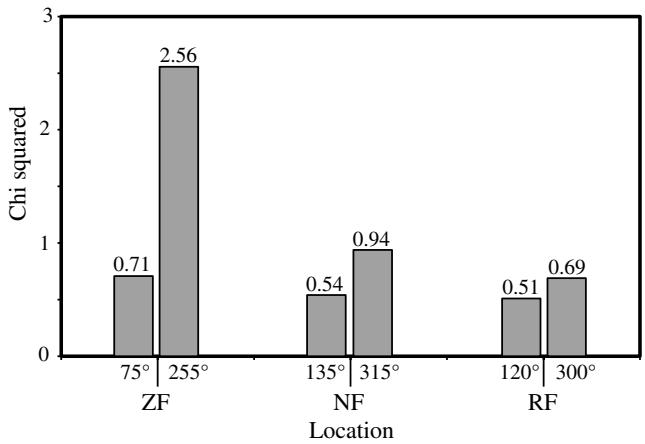

Figure 5. χ^2 comparison between our best overall candidates RF, NF, and the previously suggested ZF (Zahibo *et al.*, 2003) (see Table 3). Smaller bars represent fault candidates that are better fitting to the 1867 Virgin Island fault (see the section A Method to Quantitatively Compare between Possible Epicenters and Fault Rupture Parameters for explanation). According to this test, RF and NF are clearly better fitting than ZF (see the section The 1867 Earthquake Suggested Epicenter and Fault Parameters for details). Furthermore, southeast trending faults (strikes 120° and 135°) are a better fit, suggesting a drop in the southwest side of the fault.

normal faulting. Additional analysis of bathymetry, seismic reflection, and GPS velocities is required to better define the regional deformation pattern.

The 1867 Earthquake Suggested Epicenter and Fault Parameters

Table 3 summarizes the parameters of the two best-fitting faults (RF, North fault [NF]) and the previously suggested ZF. Figure 5 compares their chi-squared fit to observations with the previously determined source fault from hydrodynamic models (Zahibo *et al.*, 2003). Both RF and NF are better fit than ZF. Although it appears that ZF is a better candidate with respect to reported tsunami sites farther away in the Lesser Antilles (sites 4–10 in Table 1), RF and NF are much better candidates with respect to sites in the U.S. Virgin Islands and Puerto Rico (0–3 in Table 1). In both simulated RF and NF a southeast striking fault (120°, 135°) fits better than a northwest striking fault (300°, 315°) indicating that the northeast part of the fault was uplifted. Figure 6 shows plots of maximum sea level from RF, illustrating what the 1867 tsunami might have looked like. Table 1 (calculated relative amplitude) lists maximum sea levels from RF at the historical locations used for comparison in this study. Plots and values from NF are very similar. Note the high wave amplitude along the south shore of Vieques in agreement with Reid and Taber (1920), who report that "immediately after the shock a high wave broke on the south side of Viequez, and later washed its northern shore." There could be several reasons why tsunami deposits from the 1867 were not found in core analysis from the Lagoona Playa Grande (Woodruff *et al.*, 2008) tsunami deposits on the southwest coast of the island (LPG in Fig. 2) (J. Woodruff, personal comm., 2009). First, Woodruff *et al.* could not differentiate between deposits from tsunamis and hurricanes. Second, there were many events during the past 200 yrs, but only two category 5 hurricanes (1899 and 1963) could be identified in the cores with certainty. The 1899 deposits could be mixed with the 1867 deposits. Third, the 1867 tsunami followed three weeks after a category 4 hurricane in the area. Finally, the barrier between the lagoon and the sea is 2–3 m high, and the lagoon is located at the western edge of the calculated flooded coast (compare Figs. 2 and 6) beyond the wide platform south of Vieques.

Figures 7 and 8 show the marigrams from RF and NF, respectively, in places along the Caribbean and the Lesser Antilles, shown in Table 1 and Figure 1, including St. Thomas. In all marigrams for RF and NF, the leading propagating wave is a depression phase (ocean withdrawal), followed by an elevation phase (flooding), in agreement with observations (Reid and Taber 1920; O'Loughlin and Lander, 2003). The marigrams shown in Zahibo *et al.* (2003) indicate a leading elevation phase in most of the locations tested, further undermining the proposed epicenter location and suggested thrust motion.

Figure 9 shows that for marigrams generated from RF with a strike of 300° the leading propagating wave in all sites is a depression phase as well. The marigram for St. Thomas shows an immediate withdrawal, which is compatible with two eyewitness reports cited by Reid and Taber (1920). We are, therefore, unable to determine whether the southwest side of the fault was the one to drop due to the earthquake (strike 120°) or vice versa (strike 300°) based on the marigrams. In addition, although the bathymetry of the basin is more compatible with a drop of the southwest side of the fault, the tilted strata at the eastern tip of Vieques and the presence of El-Seco promontory are more compatible with a rising southwest side of the fault. Seismic profiles across the fault (Fig. 10) are inconclusive.

Table 3

Epicenter Location and Fault Parameters for the Best-Fitting Candidates and ZF

Fault	Longitude (°E)	Latitude (°N)	Length (km)	Width (km)	Slip (m)	Strike (°)	Rake (°)	Dip (°)	χ^2 Far	χ^2 Close	χ^2 Total
NF	−65	18.2	50	25	6	135/315	−45	45	0.4087	0.1325	0.5412
RF	−65	18.167	50	25	6	120/300	−45	45	0.4337	0.0753	0.509
ZF	−65	18	50	25	6	75/255	−45	90	0.3309	0.3772	0.7081

NF, North fault; RF, Reid fault; ZF, Zahibo fault. Source locations are measured in the center of each finite fault. Source depth for all faults is 1000 m, taken at the top of the fault plane. The dimensions of ZF were reduced to fit the hypothesized M 7.5.

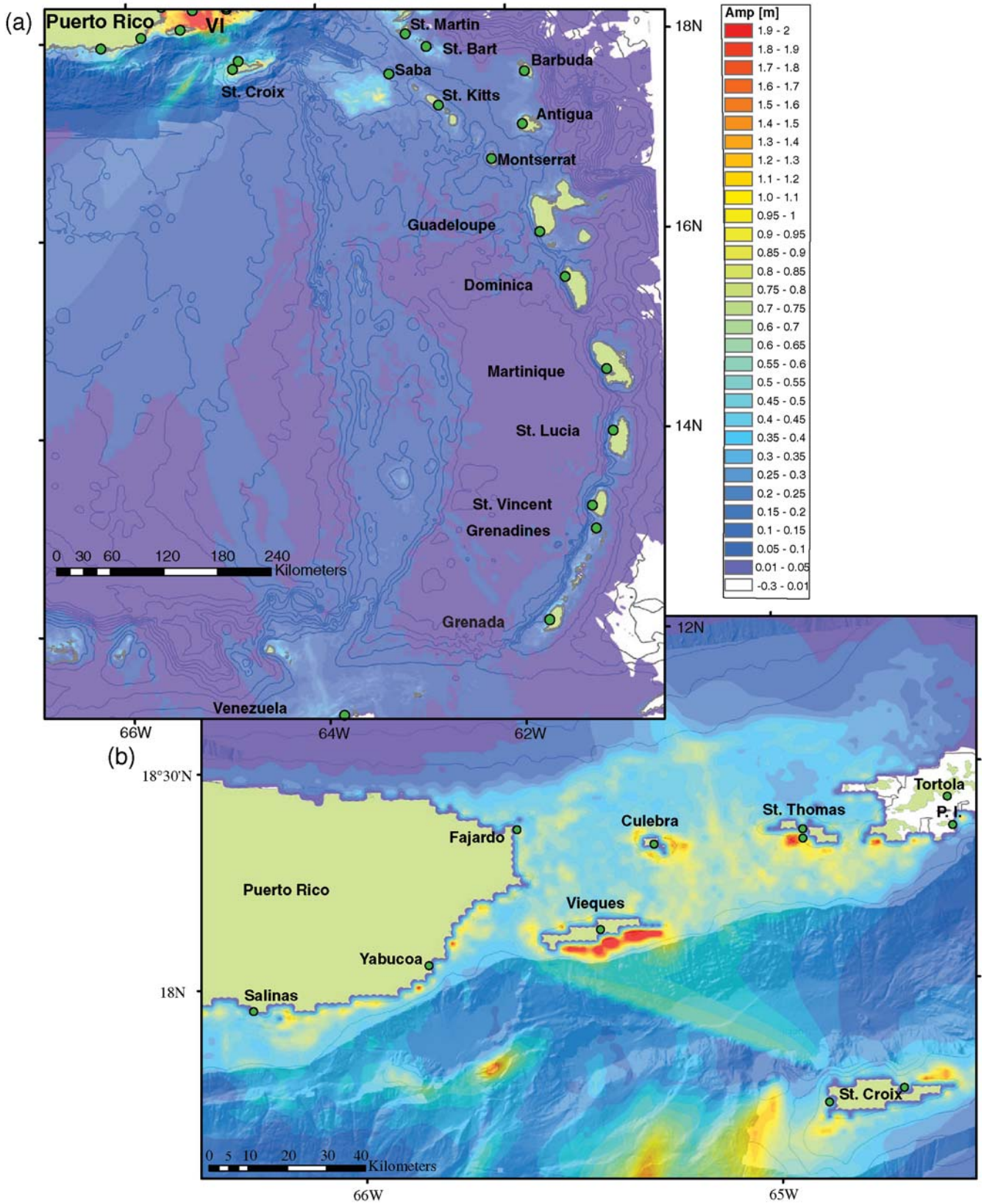

Figure 6. Maximum wave amplitude from an earthquake source located in RF (see source 14 in Fig. 2 and Table 3 for fault parameters). (a) Entire region of study. (b) Region of Puerto Rico and the Virgin Islands. The scale ranges from 0 to 2 m. VI is Virgin Islands; PI is Peter Island.

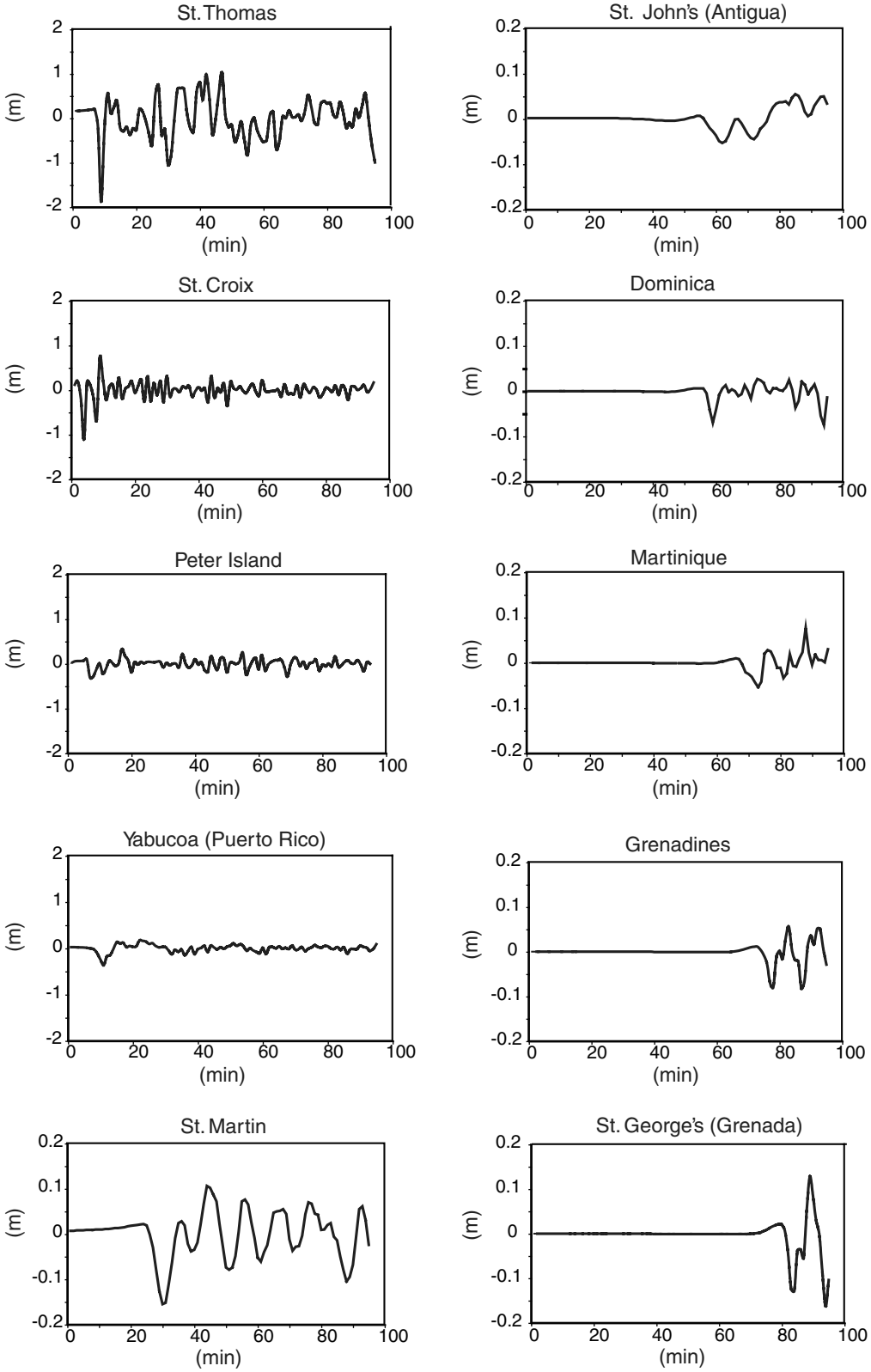

Figure 7. Marigrams from RF (see Table 3), computed at several coastal locations described in Table 1 and shown in Figure 1 (horizontal axis is the time and vertical axis is water surface elevation). As can be seen, the leading propagating wave in all sites is a depression phase, in agreement with historical reports. The amplitudes of the marigrams were calculated at the centers of the crosses at the coordinates given in Table 1. The amplitudes of the marigrams were not normalized to water depth using Green's law.

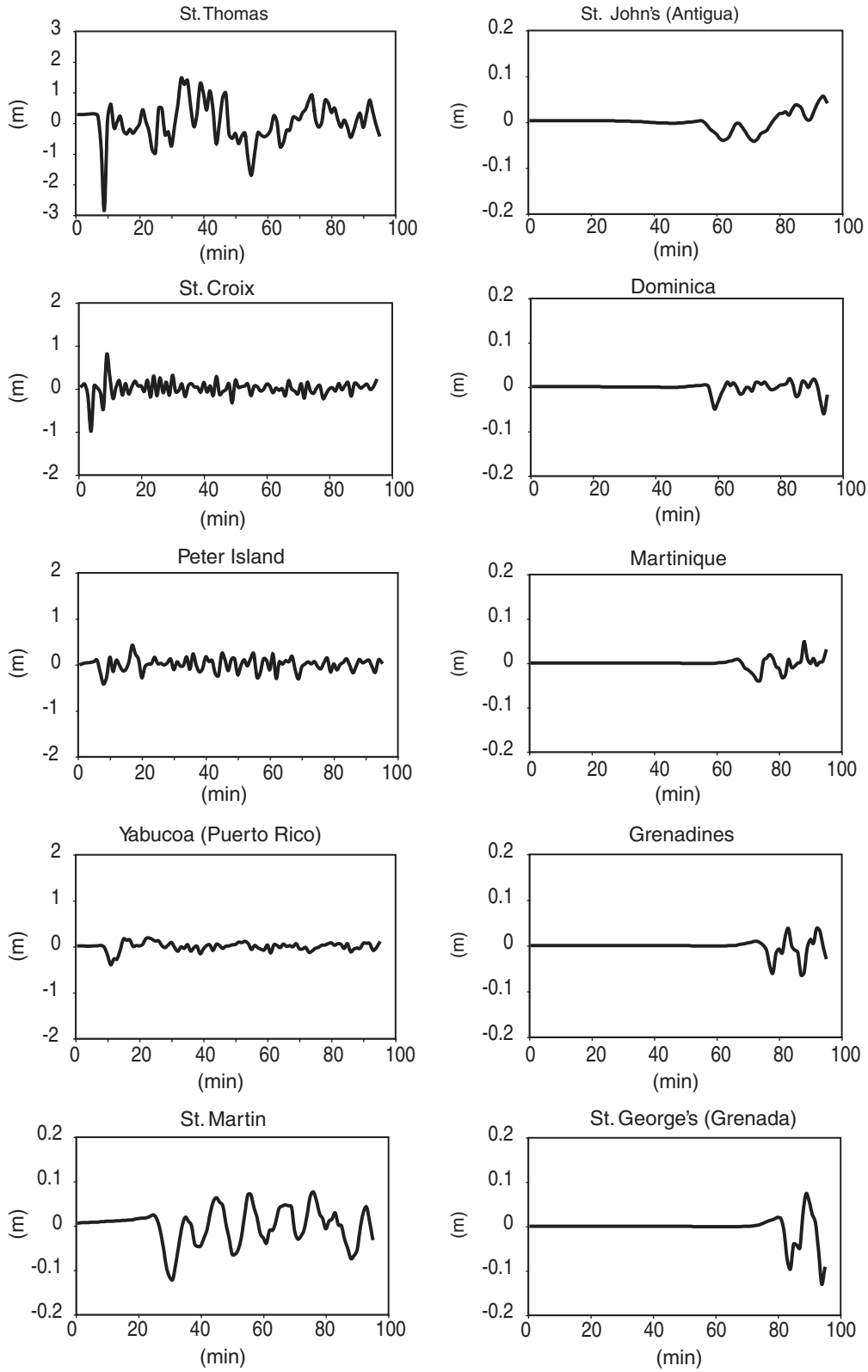

Figure 8. Marigrams from NF (see Table 3), computed at several coastal locations described in Table 1 and shown in Figure 1 (horizontal axis is the time and vertical axis is water surface elevation). As can be seen, the leading propagating wave in all sites is a depression phase, in agreement with historical reports.

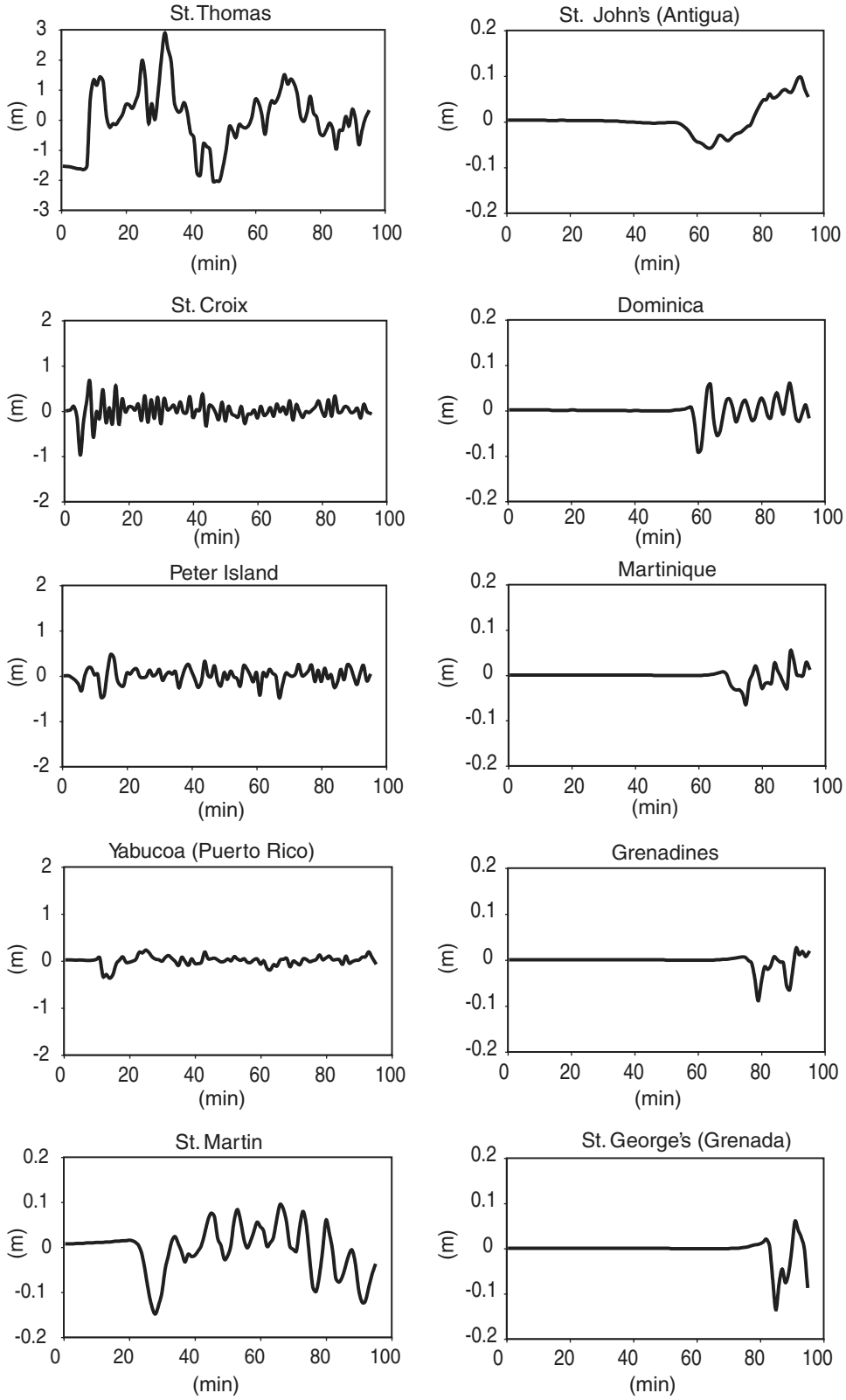

Figure 9. Same as Figure 7, but with a strike of 300°. As can be seen, the leading propagating wave in all sites is a depression phase, in agreement with historical reports. Note the depression forming at the time of the rupture on the marigram of St. Thomas. This is because St. Thomas is <25 km from the rupturing fault, and the northwest side of the fault is assumed to subside in this model. Reid and Taber (1920) quote two U.S. Navy eyewitness reports observing the water to have rushed out immediately after the first shock.

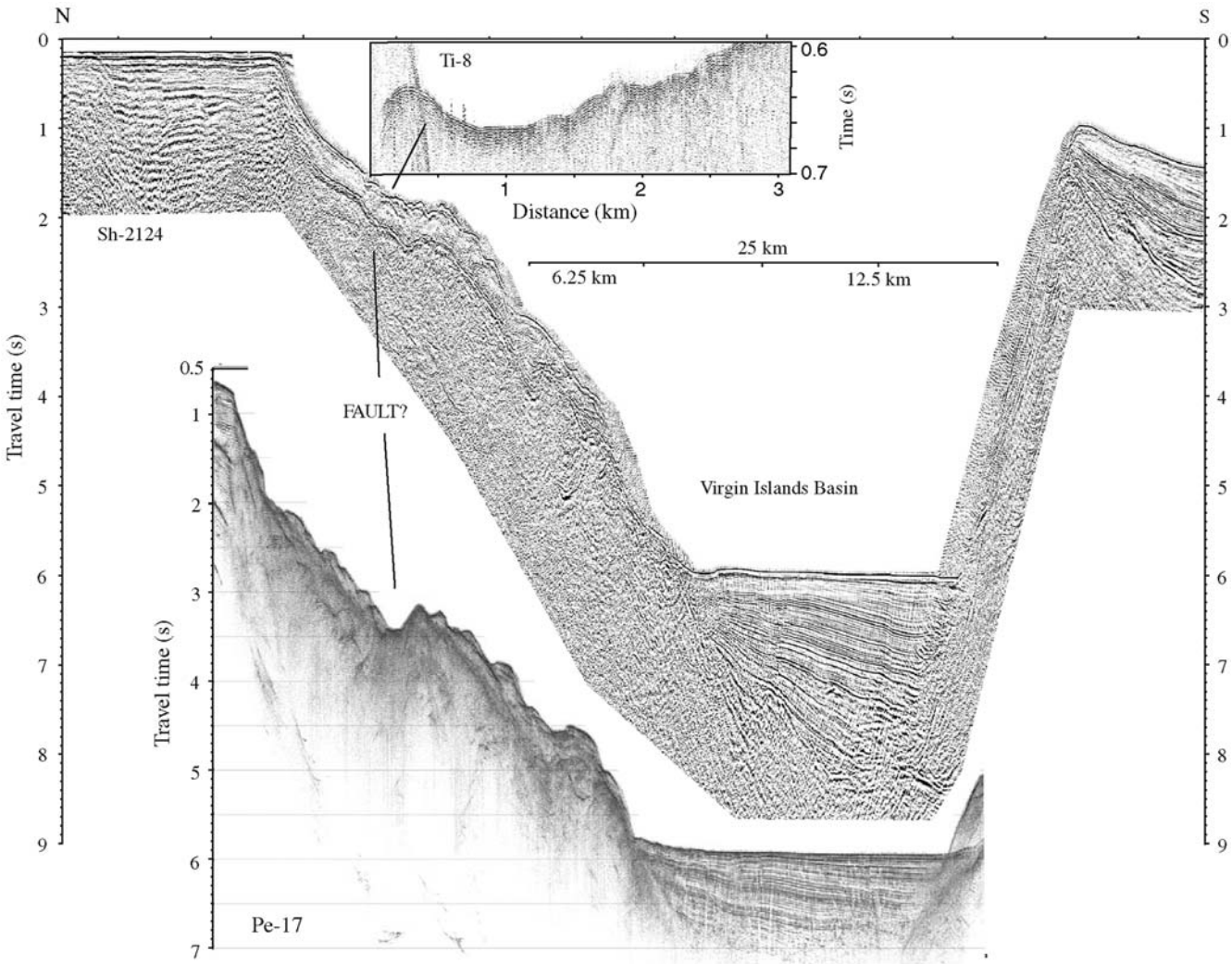

Figure 10. Seismic profiles crossing the proposed rupture of the 1867 earthquake and tsunami (see Fig. 2 for location). The difference in resolution and penetration between the lines is due to different sound sources (see the Data and Resources section).

Geophysical Evidence for the 1867 Earthquake Suggested Epicenter

RF is located only 7 km north of a potential active fault observed in geological and geophysical data (heavy dashed line marked 1867? in Fig. 2). The surface expression of the fault is oriented 110°. It is a hanging valley, which cuts the northern wall of the Virgin Islands basin diagonally and which disrupts the drainage system along the basin wall. The valley, a 15 × 10 km area of the wall below the hanging valley appears disrupted in the bathymetry (Fig. 2) and in crossing seismic lines (Fig. 10). This hanging valley may be the surface expression of the 1867 rupture. It may continue northwestward onto the shelf isolating a promontory (El-Seco in Fig. 2). The fault trace may reach the northern side of the eastern tip of Vieques, where a tilted Pleistocene (?) carbonate platform is uplifted (Vaughan, 1923; Meyerhoff, 1927). However, mulitbeam bathymetry (Fig. 3) and seismic profiles on the shelf (not shown) do not show a fault scarp between Vieques and El-Seco promontory or anywhere else on the shelf between St. Thomas, Cuelebra, and Vieques. The lack of morphological and geophysical evidence for a fault rupture on the shelf may be due to the high rate of coral growth (1–1.5 m/100 yr; Macintyre *et al.*, 1977; van Moorsel, 1985) or the fact that not the entire fault ruptures the surface (Wells and Coopersmith, 1994).

Donnelly (1965) proposed the presence of an active fault at orientation of 345° with a drop on the northeast side crossing the shelf in the vicinity of Sail Rock (marked DF in Fig. 2). Multibeam bathymetry, HRES seismic profiles, and a dive have failed to identify a fault, and the step in the seafloor disappears 8 km south of Sail Rock and does not reach the shelf edge (Fig. 2).

Other lineated disruptions in the morphology of the basin can be detected in the multibeam bathymetry map (Fig. 2). Although one of these morphological lineaments could give rise to a strong second tremor ~10 min after the first tremor (Reid and Taber, 1920), their locations could not generate the observed tsunami (Fig. 3).

Seismic reflection profiles across the Virgin Islands basin show an asymmetric sediment fill, which thickens to the south (Fig. 10). This would indicate that throughout geologic history, the southern boundary of the basin could have been significantly more active than the northern boundary. However, presently, microseismic activity is centered along the northern wall of the basin (Frankel *et al.*, 1980; Puerto Rico Seismic Network catalog, http://www.prsn.uprm.edu/English/index.php); the source of the 1867 tsunami appears to have been along that side of the basin. In addition, the deepest depression of Anegada Passage (−4533 m) is located at the base of the northern wall of the Virgin Islands basin and may have a geometric relationship to the proposed faults on the northern wall of the basin (Fig. 2). In contrast to the northern wall of the basin, the southern wall of the basin appears to be shaped by large landslide scars (Fig. 1b). The complex fault pattern of Anegada Passage between longitudes 63.5° and 66° W further suggests changes in the locus of fault activity in this area through time.

Conclusions

Methodological tsunami simulations based upon historical reports of the 1867 Virgin Island tsunami suggest the following conclusions. First, the earthquake epicenter seems to have been along the upper part of the northern wall of the Virgin Islands basin between St. Croix and St. Thomas as previously proposed by Reid and Taber (1920). The two best-fitting epicenter locations are RF, −65° W, 18.1667° N (following Reid and Taber, 1920), and NF, −65° W, 18.2° N. NF is a better-fitting fault location for far sites along the Lesser Antilles, and RF is better fitting for nearer sites in the Virgin Islands and Puerto Rico. The most favorable fault source strikes are 120° for RF and 135° for NF, in contrast to the previously suggested 65°–90° trending faults (Reid and Taber, 1920; Zahibo *et al.*, 2003). Such strikes are compatible with a drop in the southwest side of the fault. Simulated marigrams, the region's bathymetry, and seismic profiles, however, suggest fault strikes of 300° and 315° (a drop in the northeast side of the fault) are also possible. No attempt was made in this study to combine the two suggested fault ruptures (RF and NF) to a single fault, which might have yielded better results. The best-fitting rake for both RF and NF is −45° (left lateral/normal), which is in agreement with several previous relative plate motion studies in the region. However, fault geometry deduced from detailed multibeam bathymetry is more compatible with a regional mixed right-lateral and normal faulting. In addition, the best-fitting fault slip is relatively large, further indicating that the focal mechanism had a normal component. The best-fitting fault area is relatively small, probably indicating the earthquake had a moment magnitude of ~7.2. Marigrams of both RF and NF show that the first arrival wave phase in all places was a depression, in agreement with historical reports. A detailed multibeam survey of the Anegada Passage bathymetry between St. Croix and St. Thomas reveals a hanging valley, which may correspond to our hypothesized RF (Figs. 2 and 3). The valley is oriented 110°, cuts the northern wall of the Virgin Islands basin diagonally, and disrupts the drainage along the basin wall. No clear scarp in the bathymetry was found to support our hypothesized NF in either the multibeam bathymetry or in HRES seismic profiles (e.g., Fig. 2).

It is important to note that the interpretations in this report considered relative amplitudes only and that HRES near-shore bathymetry was only available for the Virgin Islands and Puerto Rico region. HRES bathymetry of the Lesser Antilles is crucial for more accurate run-up calculations and better analysis of the possible epicenter location and fault parameters.

Data and Resources

Propagation models were calculated using the Cornell Multigrid Coupled Tsunami Model (COMCOT) developed by P. L.-F. Liu, X. Wang, S-B. Woo, Y-S. Cho, and S.B. Yoon at the School of Civil and Environmental Engineering, Cornell University (Liu *et al.*, 1998). All calculations were performed on the Arctic Region Supercomputing Center at the University of Alaska, Fairbanks, using the Tsunami Computational Portal at http://tsunamiportal.nacse.org/wizard.php (last accessed January 2010). The portal is a joint project of the Northwest Alliance for Computational Science and Engineering at Oregon State University (www.nacse.org) and the Arctic Region Supercomputing Center (www.arsc.edu) at the University of Alaska, Fairbanks.

Gray-shaded relief bathymetry map in Figure 1 and deep-water bathymetry in Figure 2 are based on multibeam bathymetry with grid resolution of 50 m collected by the University of Madrid using the Simrad EM-120 on the R/V *Hesperides* in 2005 and by the USGS using SeaBeam 2112 on the National Oceanic and Atmospheric Administration (NOAA) ship *Ron Brown* in 2006. LRES bathymetry in Figure 1 is made from NOAA/NGDC (National Geophysical Data Center) ETOPO1 1 arcmin grid of global relief data. Shallow-water bathymetry is a triangulated irregular network of ungridded single-beam bathymetry from NOAA hydrographic surveys distributed by NOAA/NGDC. Color bathymetry is multibeam bathymetry with grid resolution of 5 m collected by the USGS aboard the fishing vessel *Tiki XIV* in 2009, by Géophysique GPR International, Montreal, on contract to the University of the Virgin Islands in 2005 and by NOAA Biogeography program aboard the NOAA ship *Nancy Foster* in 2009. Gray-shaded relief bathymetry south of Vieques was collected by NOAA Biogeography program aboard the NOAA ship *Nancy Foster* in 2008 and 2009. LIDAR (light detection and ranging) -based bathymetry around Vieques and Cuelebra were collected by the U.S. Army Corps of Engineers in 2000 using the scanning hydrographic operational airborne LIDAR survey system.

Seismic reflection line Sh-24 is part of profile C2124 collected in 1974 by Shell Oil aboard the ship *Petrel* using a 1200 cu. inch airgun array and a 60-channel, 3000 m long streamer. Line Pe-17 was collected by the USGS aboard the

R/V *Pelican* in 2007 using a 35 cu. inch generated injection gun, and a 24-channel, 240 m long streamer. Line Ti-8 was collected by the USGS in 2009 aboard the vessel *Tiki XIV* using a 300 J minisparker and a single channel.

Acknowledgments

We thank Tom Logan and Elena Suleimani (Arctic Region Supercomputing Center) and Dylan Keon (Oregon State University) for assistance with running the models. Brian Andrews, Bill Danforth, Chuck Worley, and Emile Bergeron helped with data collection and processing aboard the *Tiki XIV*, and Claudia Flores helped with seismic data processing. Bill Danforth and Brian Andrews merged and gridded the other multibeam bathymetry data. Tim Battista (NOAA) and Ryan Smith (University of the Virgin Islands) provided multibeam bathymetry data on the Virgin Islands platform. Helpful reviews by Eric Geist, Bill Dillon, Bill McCann, and editor Fred Pollitz are gratefully acknowledged.

References

Aki, K., and P. G. Richards (1980). *Quantitative Seismology: Theory and Methods*, W. H. Freeman, San Francisco.

Barkan, R., U. S. ten Brink, and J. Lin (2009). Far field tsunami simulations of the 1755 Lisbon earthquake: Implications for tsunami hazard to the U.S. East Coast and the Caribbean, *Mar. Geol.* **264,** 109–122.

Donnelly, T. W. (1965). Sea-bottom morphology suggestive of post-Pleistocene tectonic activity of the eastern Greater Antilles, *Geol. Soc. Am. Bull.* **76,** 1291–1294.

Dookhan, I. (1975). *History of the Virgin Islands*, University of West Indies Press, Kingston.

Doser, D. I., C. M. Rodriguez, and C. Flores (2005). Historical earthquakes of the Puerto Rico–Virgin Islands region (1915–1963), *Spec. Pap. Geol. Soc. Am.* **385,** 103–114.

Frankel, A., W. R. McCann, and A. J. Murphy (1980). Observations from a seismic network in the Virgin Islands region: Tectonic structure and earthquake swarms, *J. Geophys. Res.* **85,** 2669–2678.

Fratantoni, D. M., R. J. Zantopp, W. E. Johns, and J. L. Miller (1997). Updated bathymetry of the Anegada–Jungfern Passage complex and implications for Atlantic inflow to the abyssal Caribbean Sea, *J. Mar. Res.* **55,** 847–860.

Gill, I., P. P. McLaughlin Jr., and D. K. Hubbard (1999). Evolution of the Neogene Kingshill Basin of St. Croix, U.S. Virgin Islands, in *Caribbean Basins*, Sedimentary Basins of the World, P. Mann (Editor), Elsevier, Amsterdam, 343–366.

Green, G. (1837). On the motion of waves in a variable canal of small depth and width, *Trans. Camb. Phil. Soc.* **6,** 457–462.

Hess, H. H., and J. C. Maxwell (1953). Caribbean research project, *Geol. Soc. Am. Bull.* **64,** 1–6.

Jany, I., K. M. Scanlon, and A. Mauffret (1990). Geological interpretation of combined Seabeam, GLORIA and seismic data from Anegada Passage (Virgin Islands, North Caribbean), *Mar. Geophys. Res.* **12,** 173–196.

Lander, J. F., L. S. Whiteside, and P. A. Lockridge (2002). A brief history of tsunamis in the Caribbean Sea, *Sci. Tsunami Haz.* **20,** 57–94.

Liu, P. L.-F., S.-B. Woo, and Y.-S. Cho (1998). Computer program for tsunami propagation and inundation, sponsored by the National Science Foundation, Cornell University, Ithaca, New York.

Lynett, P. J., T.-R. Wu, and P. L.-F. Liu (2002). Modeling wave runup with depth-integrated equations, *Coast. Eng.* **46,** 89–107.

Macintyre, I. G., R. B. Burke, and R. Stuckenrath (1977). Thickest recorded Holocene reef section, Isla Perez core hole, Alacran Reef, Mexico, *Geology* **5,** 749–754.

Matsuyama, M., J. P. Walsh, and H. Yeh (1999). The effect of bathymetry on tsunami characteristics at Sissano Lagoon, Papua New Guinea, *Geophys. Res. Lett.* **26,** 3513–3516.

McCann, W. R. (1985). On the earthquake hazards of Puerto Rico and the Virgin Islands, *Bull. Seismol. Soc. Am.* **75,** 251–262.

Meyerhoff, H. A. (1927). The physiography of the Virgin Islands, Culebra, and Vieques, New York Academy of Science, *Scientific Survey of Porto Rico and the Virgin Islands* **4,** 71–141.

Mofjeld, H. O., V. V. Titov, F. I. González, and J. C. Newman (2000). *Analytic Theory of Tsunami Wave Scattering in the Open Ocean with Application to the North Pacific Ocean*, NOAA Tech. Memo. OAR PMEL-116, NTIS: PB2002-101562, 38 pp.

Murphy, A. J., and W. R. McCann (1979). Preliminary results from a new seismic network in the northeastern Caribbean, *Bull. Seismol. Soc. Am.* **69,** 1497–1513.

O'Loughlin, K. F., and J. F. Lander (2003). *Caribbean Tsunamis*, Kluwer Academic Publishers, Dordrecht, 263 pp.

Pacheco, L. D., and L. R. Sykes (1992). Seismic moment catalog of large shallow earthquakes, 1900 to 1989, *Bull. Seismol. Soc. Am.* **82,** 1306–1349.

Reid, H. F., and S. Taber (1920). The Virgin Islands earthquakes of 1867–1868, *Bull. Seismol. Soc. Am.* **10,** 9–30.

ten Brink, U. S. (2005). Vertical motions of the Puerto Rico Trench and their cause, *J. Geophys. Res.* **110** B06404, doi 10.1029/2004JB003459.

Van Moorsel, G. W. N. M. (1985). Disturbance and growth of juvenile corals (Agaricia humilis and Agaricia agaricites, Scleractinia) in natural habitats on the reef of Curacao, *Mar. Ecol. Progr.* **24,** 99–112.

Vaughan, T. W. (1923). Stratigraphy of the Virgin Islands of the United States and of Culebra and Vieques islands, and notes on eastern Puerto Rico, *J. Wash. Acad. Sci.* **13,** 303–317.

Ward, S. (2002). Tsunamis, *Encyclopedia of Physical Science and Technology* Vol. **17**, Elsevier, Amsterdam, 175–191.

Wells, D. L., and K. J. Coppersmith (1994). New empirical relationships among magnitude, rupture length, rupture width, rupture area, and surface displacement, *Bull. Seismol. Soc. Am.* **84,** 974–1002.

Woodruff, J. D., J. P. Donnelly, D. Mohrig, and W. R. Geyer (2008). Reconstructing relative flooding intensities responsible for hurricane-induced deposits from Laguna Playa Grande, Vieques, Puerto Rico, *Geology* **36,** 391–394.

Zahibo, N., E. Pelinovsky, A. Yalciner, A. Kurkin, A. Koselkov, and A. Zaitsev (2003). The 1867 Virgin Island tsunami; observations and modeling, *Oceanol. Acta* **26,** 609–621.

Department of Geophysics and Planetary Sciences
Tel-Aviv University
Ramat Aviv, Tel-Aviv 69978, Israel
(R.B.)

USGS
Woods Hole Science Center, 384 Woods Hole Road
Woods Hole, Massachusetts 02543
utenbrink@usgs.gov
(U.t.)

Manuscript received 4 August 2009